

Modeling dislocation-related leakage currents in GaN *p-n* diodes

Cite as: J. Appl. Phys. **126**, 245705 (2019); doi: [10.1063/1.5123394](https://doi.org/10.1063/1.5123394)

Submitted: 5 August 2019 · Accepted: 21 November 2019 ·

Published Online: 30 December 2019



View Online



Export Citation



CrossMark

C. A. Robertson,^{1,a)} K. S. Qwah,¹ Y.-R. Wu,² and J. S. Speck¹

AFFILIATIONS

¹ Materials Department, University of California, Santa Barbara, California 93106, USA

² Department of Electrical Engineering, National Taiwan University, Taipei City 10617, Taiwan

^{a)}Email: christian00@umail.ucsb.edu. Tel.: +1 (214) 729-5574.

ABSTRACT

Finite element analysis software was used to model and visualize two p-n junction models: one with a single threading dislocation (TD) and a control model without a dislocation. TDs are modeled as a Gaussian distribution of trap states with an FWHM of 5 nm localized around the $r = 0$ line in a cylindrical coordination such that the linear trap state density was 1 trap/c-translation; this model allows the cylindrical symmetry of the c-plane GaN crystal orientation to be utilized to avoid more computationally intensive 3D models. It was discovered that the interaction of the charged dislocation region with the p-n junction had many notable effects. At zero bias, it was observed that the depletion region width (using the Depletion Approximation) and the maximum electric field were markedly reduced near the dislocation line. More significantly, an asymmetric reduction in the diffusion barrier for electrons ($V_{bi}^{eff} = 3.03$ eV) and holes ($V_{bi}^{eff} = 0.81$ eV) was observed due to the asymmetric nature of the dislocation band bending related to the doping. The asymmetric reductions in diffusion barriers persisted into $V_A = 2.4$ V leakage case where asymmetric current profiles for electrons and holes were also observed. Lastly, the diffusion barrier reduction resulted in an additional Shockley-Read-Hall nonradiative recombination leakage caused by a high np -product and trap state density near the intersection of the dislocation with the junction.

Published under license by AIP Publishing. <https://doi.org/10.1063/1.5123394>

I. INTRODUCTION

III-N semiconductors have been widely used in high-speed transistors,^{1–5} visible and ultraviolet (UV) optoelectronics,^{6–12} and vertical power electronics.^{13–17} The high theoretical breakdown field (~ 3.3 MV/cm) and carrier mobility (> 1000 cm²/V s) have garnered interest in the field of power electronics where energy efficiency and high voltage operation are necessary. Vertical device topologies are useful for reducing the wafer footprint of power electronics by allowing voltage to be held across epitaxially grown interfaces rather than lateral ones. One of the major challenges to the performance of GaN vertical power devices has been the ubiquitous presence of threading dislocations (TDs) in the substrates for epitaxial growth. TDs have been repeatedly shown to exacerbate catastrophic and noncatastrophic breakdown in vertical GaN devices,^{16,18,19} but the mechanisms by which this occurs have been hitherto unstudied despite being experimentally observed.

The dislocation structure in GaN has been extensively studied by high-resolution x-ray diffraction (HRXRD) and transmission

electron microscopy (TEM). Edge and mixed-type threading dislocations have been shown to be much more prevalent than their screw-type counterparts, but they all have a line vector within $\sim 10^\circ$ of the $\langle 0001 \rangle$ direction regardless of their Burger's vector, \vec{b} .^{20,21} Furthermore, the electrical nature of TD trap states in n-GaN has been shown to be a deep acceptor in the bandgap with a line density of approximately one electron trap state per c-lattice translation.^{22,23} It has also been observed that this trap state density associated with TDs results in a screening region around the dislocation as the donors interact with the trap states to create regions of significant net charge. In a simple picture, the occupied dislocation-related acceptors in an n-type material are screened by ionized donors as shown in Fig. 1. Similarly, we assume that dislocation-related donors are screened by ionized acceptors in a p-type material.

In the simplest treatment, the dislocation and space charge regions are cylindrical with constant trap state and dopant density (Fig. 1). The screening radius can be simply calculated using

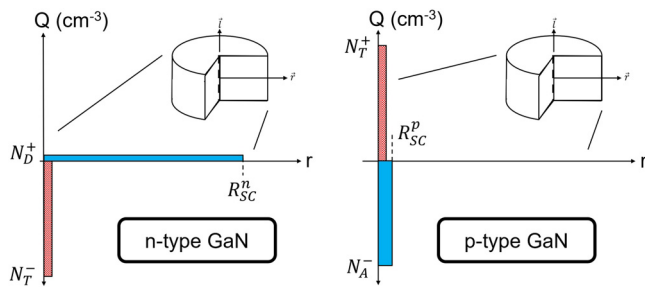


FIG. 1. Simplified representation of screening regions around a dislocation in a lightly doped ($N_D = 5 \times 10^{17} \text{ cm}^{-3}$) n-type (left) and heavily doped ($N_A = 5 \times 10^{19} \text{ cm}^{-3}$) p-type (right) GaN. Note that the charge region around the dislocation in p-type GaN is much smaller than in n-type GaN due to the high doping required to produce p-type conductivity being on the order of the density of trap states. Note that N_D^+ and N_A^- are the ionized donor and acceptor concentrations, respectively, N_T^+ and N_T^- are the ionized negative and positive trap state concentrations, respectively, and R_{SC}^n and R_{SC}^p are the screening regions in the n- and p-type regions, respectively.

Charge Neutrality and results in

$$R_{SC} = \sqrt{\rho_n * \frac{1}{\pi c}} \quad (1)$$

where ρ_n is the number of trap states per c-lattice translation, c is the c-lattice constant, and N is the uniform dopant concentration of the semiconductor. This ionization and screening of the cylindrical area of the TD line distort the energy band profiles around the dislocation with potentials of ~ 2.5 V as observed using electron holography in n-GaN.²⁴ This behavior has been attributed to the coalescence of defects around the TD core as suggested by Arslan and Browning²⁵ and observed by Müller *et al.*²⁶ The trap state energy associated with such a band bending closely matches an electron trap state of ~ 1.0 eV above the valence band maximum found in DLTS measurements;²² additionally, the trap state density is consistent with previous experimental and theoretical values of approximately one electron trap state per c-lattice translation.²⁷ From these experimental observations and theoretical predictions, it is possible to construct an accurate band structure model of n-type GaN pierced by a TD.

In contrast, a band structure model of p-type GaN that includes the treatment of TD trap states has been substantially more elusive. Electron holography analyses have found regions of negative space charge that is likely associated with screening acceptors around a donor trap state coalescing near TDs in p-GaN.²⁴ However, the high acceptor concentration needed to achieve measurable hole conductivity results in a screening region that is beyond the resolution of the holography method is likely able to measure accurately (~ 2 nm). Thus, the nature of the TD charge behavior in p-GaN remains experimentally unobserved. However, in our previous work, TDs in p-GaN act as nonradiative centers similar to n-GaN as shown by cathodoluminescence (CL) results;²⁸ thus, we assume that the TD trap states behave similarly in p- and n-type GaN.

These analyses indicate that in the unipolar bulk regions threading dislocations can be accurately described as a distribution of compensating trap states in the crystal along the TD line, but the interactions of the distortions in the band profiles of unipolar materials at a bipolar junction present an interesting physical problem that has now been modeled. In this study, a physical model is presented to treat a vertical GaN p-n junction with a TD puncturing junction. Energy band, electric field, and current flow diagrams are presented along with other plots of merit, and the mechanisms therein are discussed.

II. MODEL

In the Appendix, all relevant variables are given in alphabetical order to assist in understanding the parameters and models used in this work.

In this study, Silvaco's ATLAS modeling software was used to solve for the 2D p-n junction model shown in Fig. 2. Cylindrical coordinates were used to simplify the computational requirements by utilizing the sixfold rotational symmetry of the 3D crystal structure about the TD line vector, $\langle 0001 \rangle$, without resorting to a full 3D treatment. N_A and N_D values are chosen based on experimentally typical values for vertical GaN p-n junctions doped with Mg and Si, respectively. The model r-dimension limit of 564 nm approximates a 10^8 cm^{-2} TD density as is typical in commercially available GaN growth on either Al_2O_3 or SiC. Our TD-associated trap state region was treated as a Gaussian distribution with FWHM of 5 nm and a peak trap state density of $6.84 \times 10^{19} \text{ cm}^{-3}$. This is a close approximation of experimental observations of edge and mixed-type dislocations with coalesced charged defects^{29,30} around an electrically inactive core as shown by Müller *et al.*²⁶ and proposed by Arslan and Browning;²⁵ however, it should be noted that pure screw-type dislocations show substantially different charge profiles²⁴ and leakage characteristics³¹ that are not modeled in this work. The distribution used approximates a one electron per c-lattice translation when normalized in the z-direction. Trap energy levels within the bandgap were $E_C - 2.5$ eV and $E_V + 2.3$ eV for n- and p-type GaN, respectively. Although the energy level of the dislocation trap state in n-GaN is well-documented, the level for p-GaN is approximated as an arbitrarily deep donor state. This assumption will be discussed later.

The trap state properties are also chosen such that the minority carrier diffusion lengths and lifetimes match those given in the literature. Using the approximation of a 10^{16} cm^{-3} trap state density in the bulk away from the dislocation, a capture cross section for both electrons and holes of 10^{-12} cm^2 was chosen based on the following equations:

$$\tau = (\rho_T * \sigma * v)^{-1}, \quad (2)$$

$$L_T = \sqrt{\frac{kT}{q} * \mu * \tau}, \quad (3)$$

where τ is the minority carrier lifetime, ρ_T is the local trap concentration, σ is the trap minority carrier capture cross section, v is the minority carrier thermal velocity, L_T is the minority carrier diffusion length, and μ is the minority carrier mobility. These values resulted

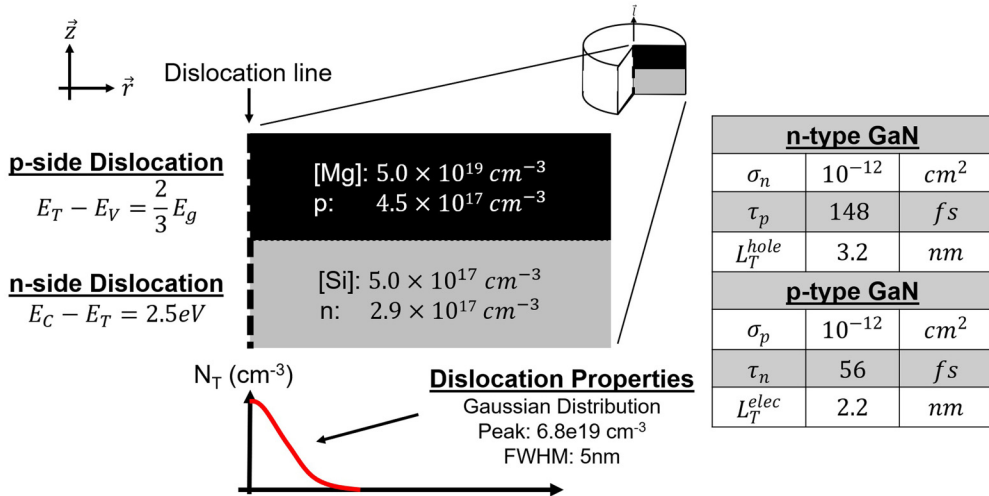


FIG. 2. A cylindrically symmetric p-n diode is modeled for this study with a Gaussian distribution of deep trap states used to represent the TD-associated traps. Typical doping densities for the p- and n-type regions are used, and, experimentally, standard hole and electron concentrations are observed in the model. The location of the trap state energy within the n-type region was based on experimental results while the p-type region was placed arbitrarily deep in the energy gap. In the right table, values for trap capture cross section (σ), minority carrier lifetime (τ), and minority carrier diffusion length (L_T) are given for the trap state region associated with the TD line. These values were chosen such that these model variables all matched experimental values as closely as possible.

in lifetimes and transfer lengths given in Table I using the minority carrier mobilities found by Kumakura *et al.*³² The bulk values for ρ_T approximate experimental observations,^{23,27,33} and the lifetimes given in this table are within the expected range for minority carrier diffusion length and lifetime^{30–33} and were observed in our diode model with no dislocation.

Using this physical model, the Poisson and steady-state Current continuity equations are solved on the mesh self-consistently using the Gummel method (Fig. 3),

$$\vec{\nabla} \cdot (\epsilon \vec{\nabla} \psi) = q(n - p - N_D^+ + N_A^-) - Q_T, \quad (4)$$

$$\nabla \cdot \vec{J}_n = -qU(n, p), \quad (5)$$

$$\nabla \cdot \vec{J}_p = qU(n, p). \quad (6)$$

In the Poisson Eq. (3), ψ is the electric potential, n and p are the electron and hole concentration, and N_D^+ and N_A^- are the ionized donor and acceptor concentrations. In the Current continuity equations, J_n and J_p are the electron and hole current densities,

TABLE I. Minority carrier lifetimes and diffusion lengths for different trap state conditions. The bulk lifetimes are within experimental parameters for minority carrier lifetimes.³⁰

	ρ_T (cm ⁻³)	τ_n	L_T^n (nm)	τ_p	L_T^p (nm)
TD core	6.84×10^{19}	56 fs	2.1	148 fs	3.2
Bulk	10^{16}	0.38 ns	178	1.01 ns	261

and $U(n, p)$ is the net recombination-generation rate. If convergence is not achieved, the solver will switch from the Gummel to the Newton-Raphson method to solve the system of equations.

In addition to these core equations, additional models are necessary to include the various behaviors of the GaN material systems and trap physics. These are discussed below.

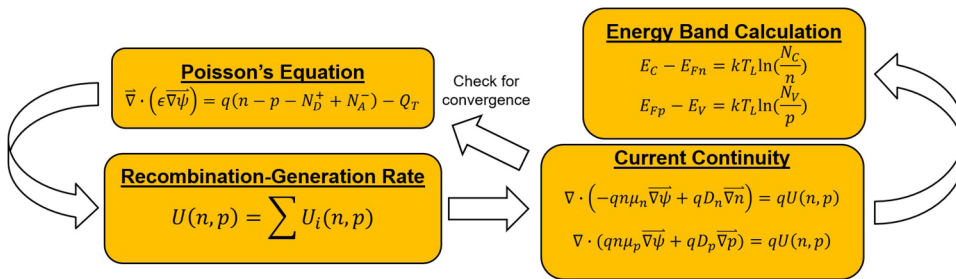
A. Incomplete ionization model

It has been well-documented experimentally that Mg_{Ga} has an activation energy of around 190 meV;^{34,35–37} thus, to accurately model p-GaN, we utilized the incomplete ionization model³⁸ to account for the thermal activation of both the donors and acceptors in GaN,

$$N_D^+ = \frac{N_D}{1 + g_n \exp\left(\frac{(E_{Fn} - (E_C - E_D))}{kT}\right)}, \quad (7)$$

$$N_A^- = \frac{N_A}{1 + g_p \exp\left(\frac{(E_A - E_V) - E_{Fp}}{kT}\right)}, \quad (8)$$

where N_D^+ and N_A^- are the ionized donor and acceptor concentrations, N_D and N_A are the donor and acceptor concentrations, g_n and g_p are the conduction and valence band degeneracies, E_{Fn} and E_{Fp} are the electron and hole quasi-Fermi levels, and $(E_C - E_D)$ and $(E_A - E_V)$ are the donor and acceptor activation energies. This model predicts that only ~1% of the Mg acceptor dopants will contribute holes to the GaN semiconductor while ~60% of the Si donors will contribute electrons. Furthermore, unintentionally doped GaN is usually slightly n-type due to the unintentional doping by oxygen. This combined



with the low activation efficiency necessitates high Mg concentrations to achieve p-type GaN experimentally.

Our model makes two basic doping assumptions. Firstly, the model uses an abrupt metallurgical junction such that there is no overlap between the p- and n-type regions of the diode. Secondly, the model does not explicitly specify any compensating defects or recombination centers in the model away from the dislocation but rather combines the holistic crystal imperfections into a minority carrier lifetime within the range of values provided in the literature.³⁰

B. Shockley-Read-Hall (SRH) trap-assisted recombination model

To model the charging and screening effects around the dislocation line, a trap ionization model was implemented. The Simmons and Taylor model (based on Shockley-Read-Hall recombination statistics)^{39–41} was used to simulate the occupancy, $f(E_T)$, and charge state density of trap states, Q_T , associated with the TD line,

$$Q_T = q(N_{tD}^+ - N_{tA}^-), \quad (9)$$

$$N_{tA}^- = \rho_T * f(E_T), \quad (10)$$

$$N_{tD}^+ = \rho_T * (1 - f(E_T)), \quad (11)$$

$$f(E_T) = \frac{\bar{n} + e_p}{e_n + \bar{n} + \bar{p} + e_p}, \quad (12)$$

$$\bar{n} = v_n \sigma_n n, \quad (13)$$

$$\bar{p} = v_p \sigma_p p, \quad (14)$$

$$e_p = v_p \sigma_p N_V \exp\left(\frac{E_V - E_T}{kT}\right), \quad (15)$$

$$e_n = v_n \sigma_n N_C \exp\left(\frac{E_T - E_C}{kT}\right). \quad (16)$$

In this system of equations, Q_T is the concentration of charged trap states, N_{tD}^+ and N_{tA}^- are the concentrations of ionized donor and acceptor trap states, ρ_T is the density of trap states, $f(E_T)$ is the Fermi occupancy function at the trap state energy level, \bar{n} and \bar{p} are the electron and hole capture rates, v_n and v_p are the thermal

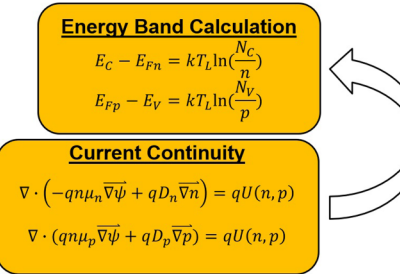


FIG. 3. Process overview of the Gummel method that was used extensively for modeling dislocation behavior; however, the Newton-Raphson methodology was used if convergence was not achieved.

velocities for electrons and holes, σ_n and σ_p are the electron and hole capture cross sections, n and p are the electron and hole concentrations, e_p and e_n are the hole and electron trap emission rates, N_V and N_C are the effective density of states for the valence and conduction bands, E_V and E_C are the valence and conduction bands, and E_T is the trap state energy level. These equations tie into the previous models given in two important ways. Firstly, the electron and hole concentrations given in (12) and (13) are functions of the quasi-Fermi levels associated with the carriers. In forward bias, these quasi-Fermi levels split near the junction and would, therefore, change the behavior of the traps in these regions. This change carrier statistics in the regions with Fermi level splitting is considered in these two equations by the inclusion of the local carrier concentrations that are functions of the quasi-Fermi levels. Secondly, as previously stated, the trap states are given a capture cross section such that the minority carrier lifetimes and minority diffusion lengths in the bulk associated with a lower concentration of these traps matches with previously found experimental evidence. The chosen values for capture cross section also come into effect here when calculating the carrier capture rate for trap occupancy. Additionally, in Eq. (8), N_{tD}^+ and N_{tA}^- represent the concentrations of ionized donor and acceptor trap states, respectively. In brief, the occupancy of the trap states within the semiconductor depends on the mechanistic rates at which that trap either captures or emits carriers. These rates are a function of the traps' position in the energy band as well as the local Fermi level that dictates the concentration of free carriers at that point. For the electron occupancy of traps given in Eq. (11), the mechanisms that will cause that trap to be occupied by an electron are the capture rate of electrons, \bar{n} , and the emission rate of holes, e_p . Thus, the steady state occupancy of the trap can be described as the ratio of these occupying rates to all of the rates on that trap state.

Equation (11) expressing the occupancy of the localized trap state is simply a rewritten form of the SRH recombination equation with the coefficients rewritten to more explicitly represent carrier emission and capture.

Additionally, Shockley-Read-Hall⁴¹ recombination rates are used directly to model trap-assisted recombination rates using the following equation:

$$U_{SRH} = \frac{pn - n_i^2}{\tau_n \left[p + n_i \exp\left(\frac{E_i - E_T}{kT}\right) \right] + \tau_p \left[n + n_i \exp\left(\frac{E_T - E_i}{kT}\right) \right]}, \quad (17)$$

where U_{SRH} is the Shockley-Read-Hall recombination rate, p and n

are the hole and electron concentrations, n_i is the intrinsic carrier concentration, τ_n and τ_p are the electron and hole lifetimes, E_i is in the intrinsic energy level, and E_T is the trap state energy level.

III. RESULTS

A. Zero bias model

In Figs. 4(a) and 4(b), the modeled band diagram of a GaN *p-n* junction around a TD is presented. The TD screening region permeates much further into the n-GaN region than the p-GaN region due to the screening behavior of lightly vs heavily doped material. This reduced area of influence of the TD within the p-GaN compared to the n-GaN means that any influence of the screening region on p-n junction leakage current is minimal in the p-type region of the device. Furthermore, this means that as power devices push toward lower drift region doping levels to hold large reverse voltages, the effects of the TD on the leakage associated with this screening region will similarly be amplified. It can also be seen that the band bending observed on the heavily doped p-side

of the junction is substantially less than the n-side despite their trap energy levels being similarly distanced from their respective energy bands. On the p-side of the junction, the density of acceptors and trap states are on the same order of magnitude; thus, there is little band bending behavior as the net charge in this region will be lower as the intentional acceptors can almost locally compensate the dislocation-related donor trap states.

In Figs. 4(c) and 4(d), the contours of the conduction and valence bands, respectively, are shown separately from the full band diagram construction. In this construction, the asymmetry of the built-in voltage reduction on the n- and p-type sides of the junction is easier to observe. The difference in diffusion barrier height can be given by

$$\Delta V_{bi} = V_{bi} - V_{bi,eff}, \quad (18)$$

where V_{bi} is the bulk built-in potential and $V_{bi,eff}$ is the effective potential at the TD. On the n-type side, this is only 270 meV; this small reduction in the electron diffusion barrier is contrasted with

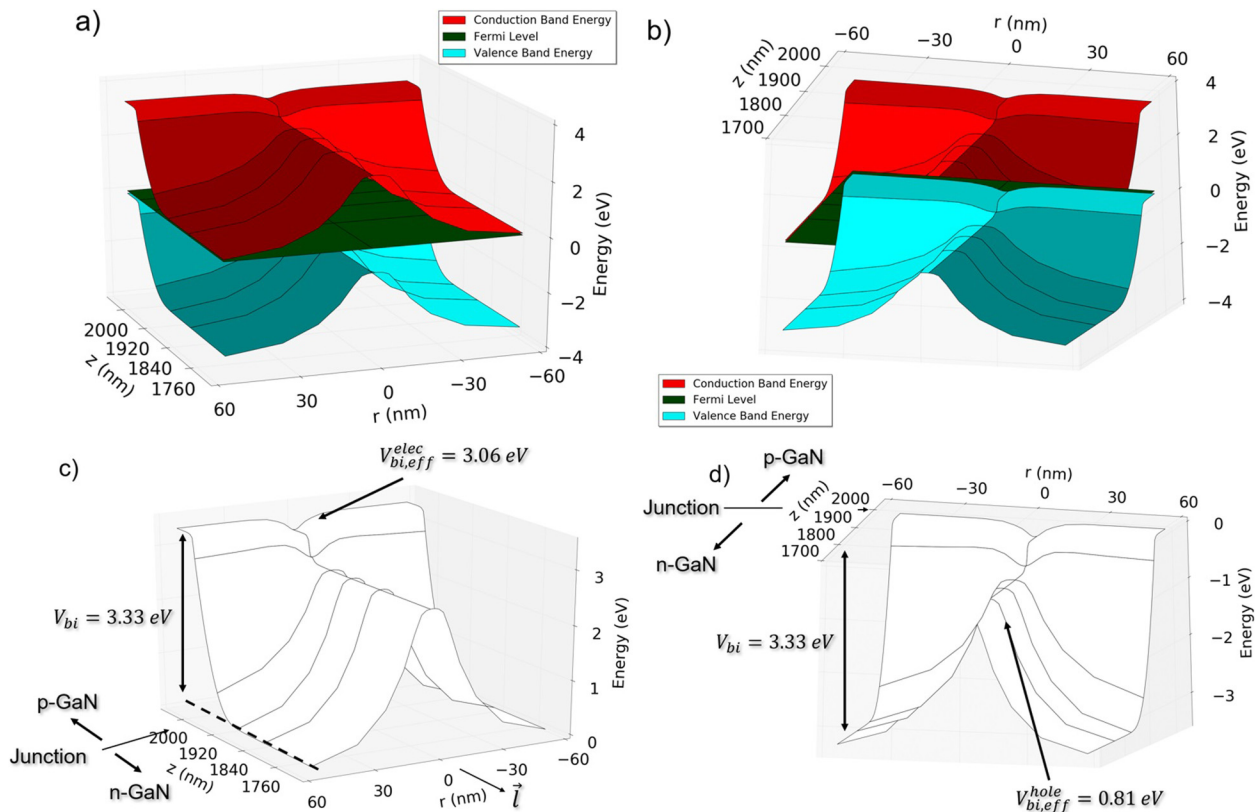


FIG. 4. (a) The full 3D zero bias band diagram of the p-n junction looking from the n-side down the dislocation line to clearly show the distortion of the band diagram around the TD line that reduces the barrier to diffusive electron current. (b) The full 3D zero bias band diagram of the p-n junction rotated such that the perspective looks down the TD from the p-side. This shows more clearly the barrier to hole diffusive current and how the barriers to diffusive currents are asymmetric at the junction. (c) The 3D zero bias band diagram of the p-n junction conduction band numerically annotated to demonstrate the reduction in the electron diffusion barrier around the dislocation. (d) The 3D zero bias band diagram of the p-n junction valence band numerically annotated to demonstrate the marked reduction in hole diffusion barrier around the dislocation. Note that for all figures in this work the metallurgical junction of the diode is at $z = 2 \mu\text{m}$.

the marked reduction in the barrier (2.52 eV) for holes. This result foreshadows that this structure should leak substantially more holes than electrons in forward bias since the equilibrium built-in potentials are asymmetric.

In Fig. 5(a), the 2D electric field colormap of the zero bias p-n junction is shown. The confluence of the screening and depletion region electric fields correlates to a marked reduction in the electric field magnitude near the dislocation core. Under forward bias, this

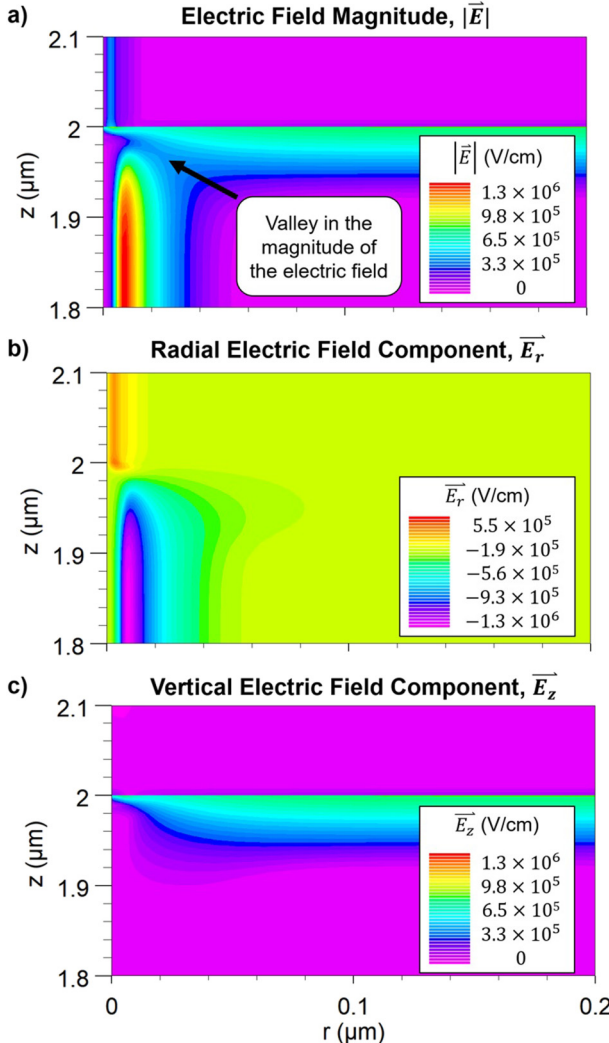


FIG. 5. Electric field colormaps showing the (a) magnitude, (b) radial, and (c) z-direction components. Note that at the intersection of the screening and depletion regions there is a valley in the magnitude of the electric field labeled in (a). Additionally, it can also be seen that near the intersection, the electric field magnitude approaches zero where the maximum screening field would intersect with the maximum depletion electric field. Note that in (c), the z-component of the electric field quickly approaches the field profile of a similar p-n junction with no dislocation (e.g., at a distance $r \approx 0.05 \mu\text{m}$).

region of reduced electric field enhances the diffusive current flow as will be shown in Sec. III B. The potential peak appears in the core of TD. Therefore, the electric field, which is the differential of potential, is zero as expected.

In Fig. 6, the depletion region width is plotted with respect to distance from the TD core. Near the TD, the depletion width is reduced by 67%. Furthermore, in the inset of the plot, it can be observed that the maximum junction electric field is similarly reduced by 37%. These two factors result in a substantially reduced barrier to diffusive current across the junction.

B. Leakage regime (2.4 V forward bias)

At ($V = 2.4$ V), high TD density GaN p-n diodes have measurable leakage currents, and these currents can be reliably observed in standard computational models without problems with numerical noise.

In Fig. 7, carrier current flow diagrams are presented. The flow of holes and electrons is almost symmetric on the p- and n-type sides of the junction, respectively. It has been previously observed at zero bias that the depletion width of the device reduces drastically with proximity to the TD, and in forward bias, this barrier reduction facilitates forward diffusive current to the region near the intersection. With a reduction in this barrier near the TD, carriers in the bulk regions of the device bypass the bulk depletion field by moving through this region. Once both carriers are confined together in this region within the device, they will rapidly recombine [Eq. (16)]. Lastly, it is significant to note that the hole current from the p-type side of the junction intrudes much further into the n-GaN TD than electrons into the p-GaN. This phenomenon will be discussed further in the Discussion section.

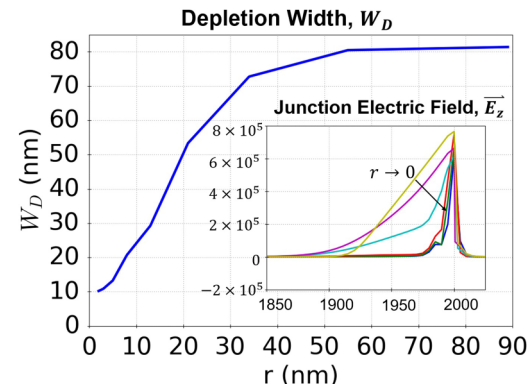


FIG. 6. Plot of the depletion region width (calculated using the Depletion Approximation) changing with proximity to the TD core. Inset into the plot are the profiles of $\rightarrow E_z$ approaching the dislocation core ($r = 0$) that are responsible for the formation of the junction depletion region. Note that near the TD ($r = 0$) both the maximum overset $\rightarrow E_z$ and depletion widths are reduced, thereby creating a reduced barrier to diffusion current through this region. Additionally, note that W_D far away from the dislocation line approaches the value derived from basic depletion calculations for a p-n junction with no dislocation.

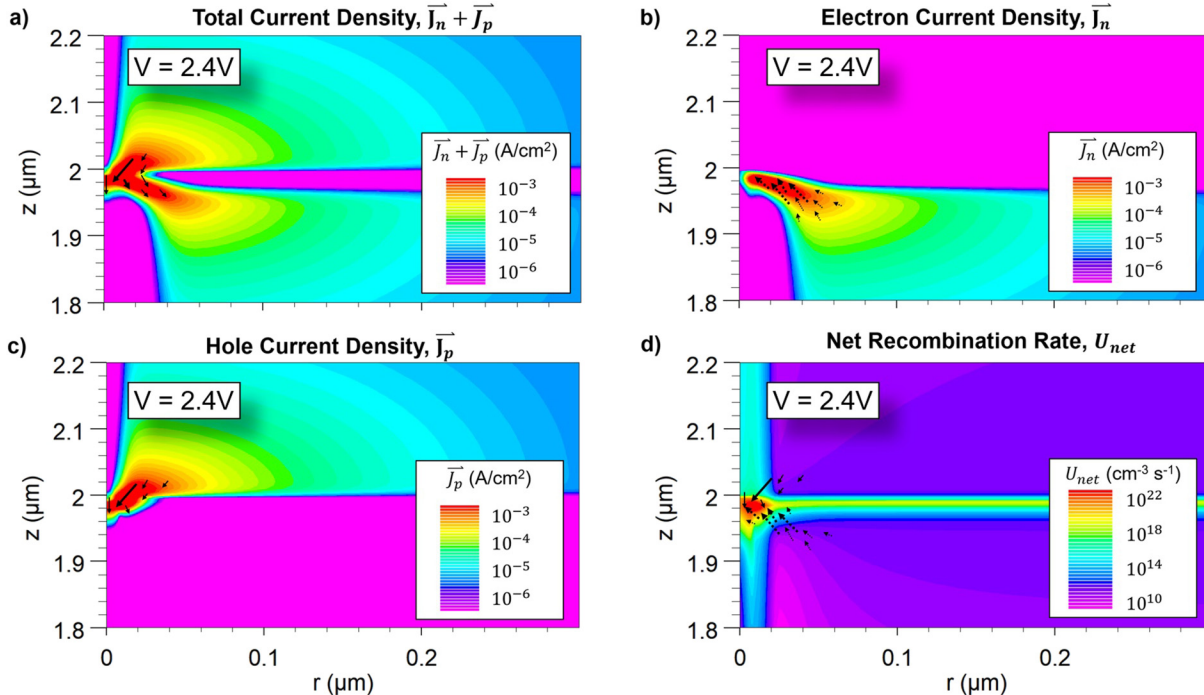


FIG. 7. Carrier transport diagrams in the leakage regime. (a) The total conduction current density for the vertical diode punctured by a threading dislocation. Note that there is current on both sides of the junction mediated by the intersection. (b) The electron current density showing the flow from the bulk of the n-GaN through the intersection and into the dislocation trap region on the p-type side. (c) The hole current density showing the flow of holes in similar magnitude to the flow of electrons. However, the holes appear to intrude much further into the n-GaN region than the electrons into the p-GaN region. (d) Net recombination rate diagram showing a wide and strong area of recombination near the intersection and around the TD in the bulk. This recombination center at the intersection will be discussed further in the “Discussion” section.

In Fig. 8, it can be clearly seen that the intersection mediates leakage current at subturn-on voltages thereby allowing current to flow through the region of reduced depletion due to the distortion in the energy band diagrams around the TD. The contrast is particularly apparent when comparing the current vectors near the TD to those far away from the dislocation at $V = 2.4$ V. Away from the TD, there is negligible current flow as would be expected in an ideal diode; however, near the TD, the current density magnitude exponentially increases as the flow of carriers moves through the region of influence of the TD.

C. J-V characteristics

I-V curves were also simulated for this model and were compared to a control diode with no dislocation region. These I-V curves were normalized to a 3D model structure with cylindrical symmetry to obtain current density (Fig. 9).

When compared to an ideal diode, the diode with the dislocation puncturing the metallurgical junction displays quantifiably higher leakage current before turn-on. After turn-on, the effects of the dislocation on the carrier transport get screened by the injected carriers at forward bias, and this effect can be seen in both the J-V curves as well as the 2D models (Fig. 7).

In Fig. 9, the ratio between the current densities of a diode with and without a TD is plotted with the models’ J-V data using the following formula:

$$\Gamma = \frac{J_{TD} - J_{noTD}}{J_{noTD}}, \quad (19)$$

where Γ is the leakage ratio, J_{TD} is the current density of a $p-n$ diode with a TD, and J_{noTD} is the current density of the ideal $p-n$ diode. The leakage current contributes substantially more current before turn-on after which the dislocation has been screened by the forward bias current. These current ratios match very closely with previous experimental work analyzing leakage current in vertical $p-n$ junctions in GaN.^{42–45}

IV. DISCUSSION

A. Pinning behavior at the dislocation

Our results demonstrate that the previously observed small potential profiles around TDs in p-GaN²⁴ are due to the necessary doping required to obtain p-type conduction. Since the concentration of acceptors in p-type GaN ($N_A = 5 \times 10^{19} \text{ cm}^{-3}$) is on the order of trap state density near the dislocation core

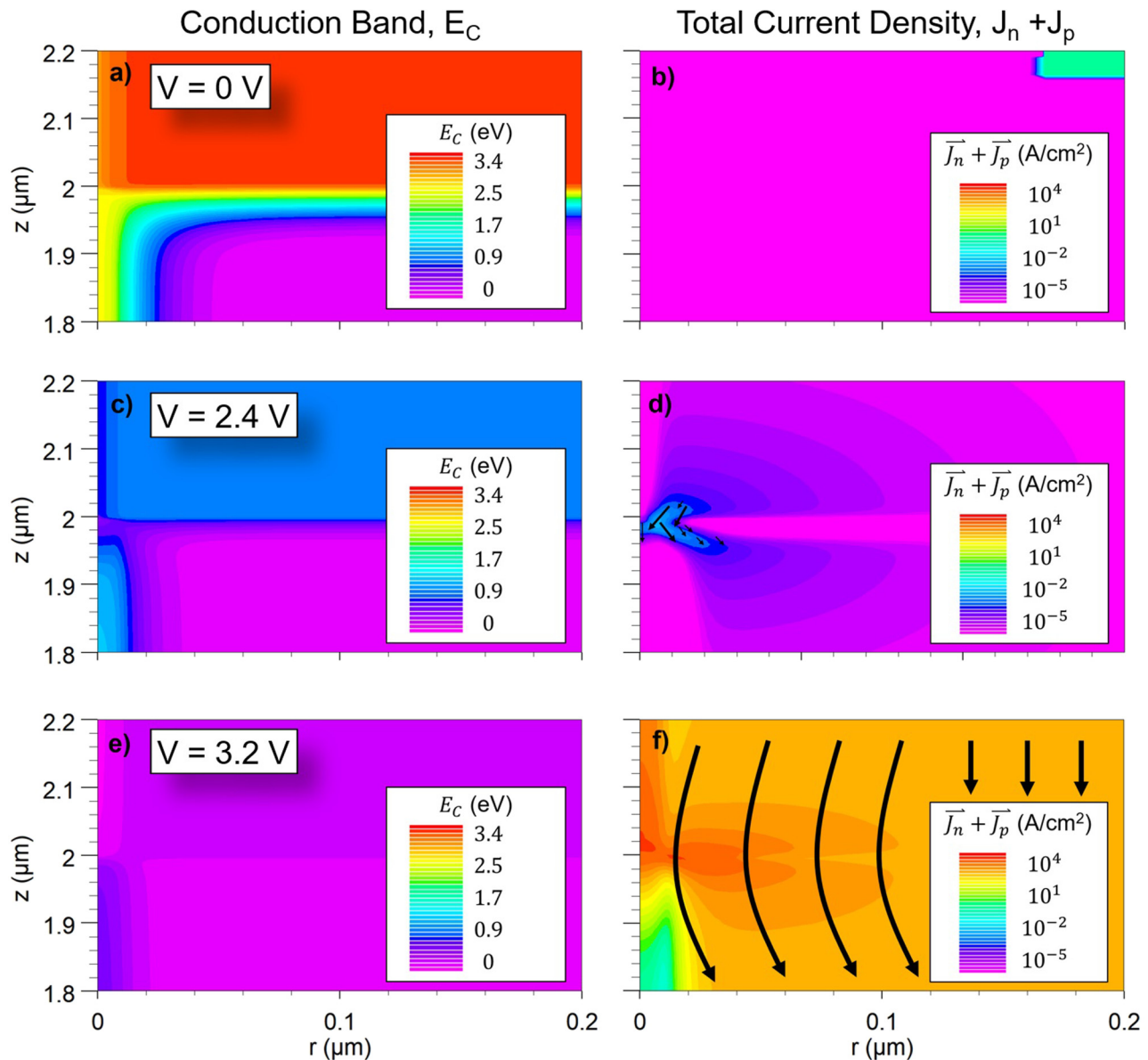


FIG. 8. Conduction band diagrams for (a) 0 V, (c) 2.4 V, and (e) 3.2 V forward bias and current density plots for (b) 0 V, (d) 2.4 V, and (f) 3.2 V forward bias. From these figures, note that the collapse in both the junction and screening electric field correlates to an increase in both the junction and TD mediated currents densities until full turn-on.

($\rho_{T,\max} = 6.84 \times 10^{19} \text{ cm}^{-3}$), the net charge in the TD region in p-GaN is less than the net charge in the n-GaN where the donor concentration is much smaller ($N_D = 5 \times 10^{17} \text{ cm}^{-3}$). This reduction in the net charge density in p-GaN directly correlates to the reduction in the associated dislocation band bending around those dislocations and results in a 100% hole occupancy of the dislocation-related trap states. It is significant to note that the trap states in the lightly doped n-GaN region of the diode are

not fully occupied near the TD, thus causing the hump in the charge concentration profile, as shown in the lower left corner of Fig. 10.

Furthermore, our results also demonstrate that the lightly doped, n-type side of the p-n junction does not actually physically pin the Fermi level at the trap state either. The low donor concentration is physically unable to compensate the trap states without bending the bands such that the trap state remains at

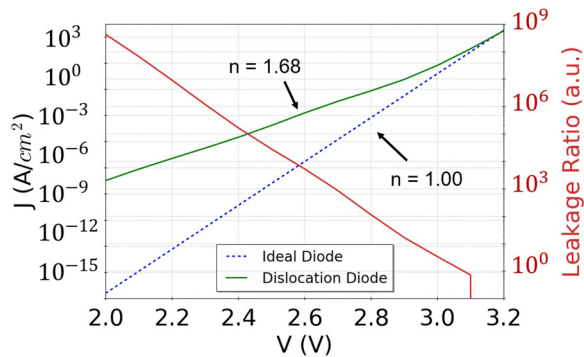


FIG. 9. Voltage sweep analysis for the diode studied in this work against an ideal GaN p-n diode of the same geometry. The left axis shows the current density of the diode as well as annotations indicating the ideality factors of the diode. The right axis shows the ratio of the current in the diode with a dislocation to one without a dislocation thereby showing a leakage ratio associated with a sample having a 10^8 cm^{-2} threading dislocation density as is typical on heteroepitaxially grown GaN-on-sapphire.

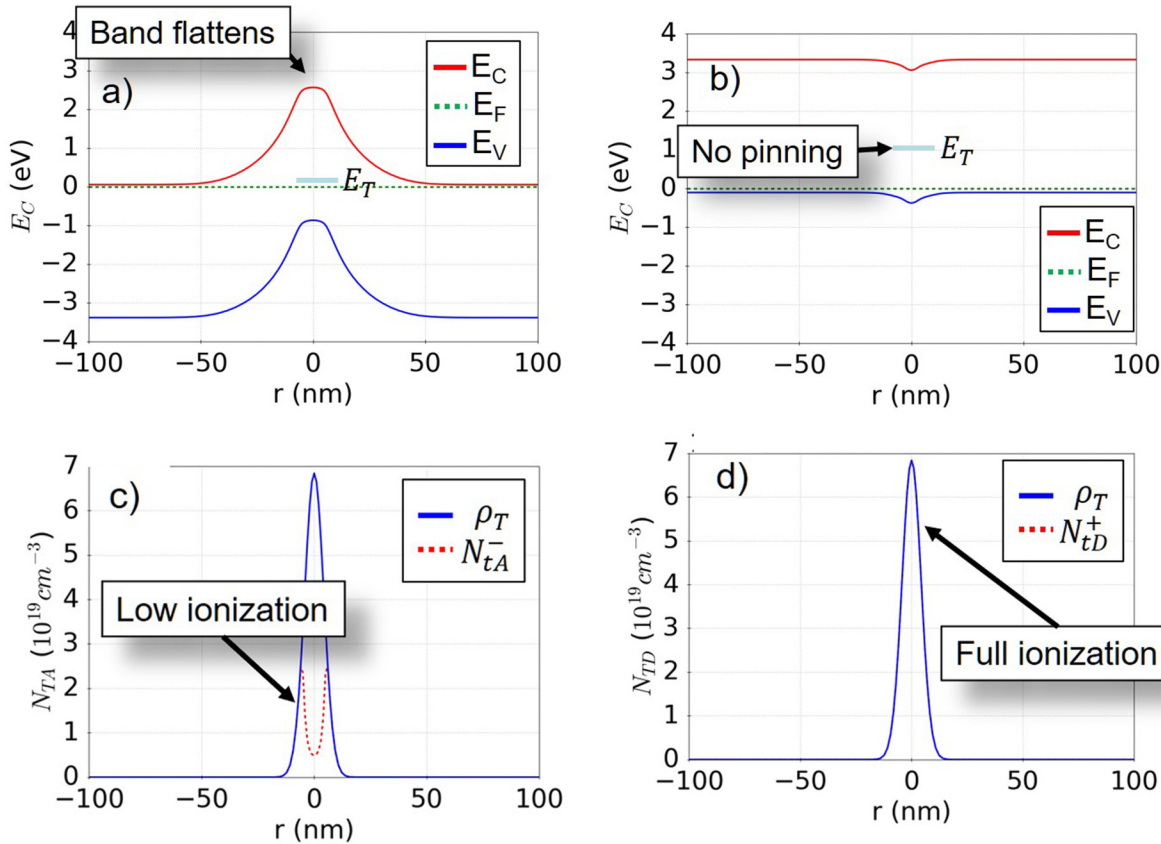


FIG. 10. Band diagrams for (a) lightly doped n-GaN and (b) heavily doped p-GaN around a TD. In the bottom row are also shown the charge densities for (c) lightly doped n-GaN and (d) heavily doped p-GaN. Note that in the lightly doped n-GaN, the band flattens near the dislocation indicating a very low electric field and reflecting a low occupancy as also indicated in the charge density graph in (c).

or below the Fermi level. Although graphical representations appear to have the trap state pinned at the Fermi energy, it is in fact 67 meV above the trap energy level. Using Fermi statistics

$$f(E) = \frac{1}{\exp\left(\frac{E_T - E_F}{kT}\right) + 1}, \quad (20)$$

it can be calculated that the occupancy of a trap state located 67 meV above the Fermi level will be $\sim 8\%$, which matches the occupancy given by the model.

B. Major mechanisms of leakage

The results presented clearly demonstrate a strong leakage mechanism at the intersection where the dislocation and metallurgical junction interact; however, additional studies are necessary to fully verify the effect of lightly doped regions with TDs on p-n junction leakage.

1. Leakage in n+p diode

The first exploratory model inverted the weight of the doping to create an n+p junction rather than a p+n junction. This model verified that it is the lightly doped region of the diode that mediates the most leakage; in Fig. 11(a), the TD on the p-type side (which is now lightly doped with $N_A = 5 \times 10^{17} \text{ cm}^{-3}$) carries a significant amount of electron current with the same partial occupancy and band flattening behavior observed in our main model. Furthermore, this current goes substantially further into the p-type region through the TD, which indicates that carriers in these regions are more likely inhibited by their mobility as would be predicted if they were acting as majority carriers in these regions.

C. p-GaN trap state energy dependence

As was previously stated, the precise location of the trap energy level for TDs in p-GaN is not known; thus, models looking at p-n junctions with different p-GaN TD trap energy levels were simulated. It was observed that the trap state level of the p-type side was largely irrelevant to the presence of previously observed leakage mechanisms. This finding indicates that although the energy level for TD traps in p-GaN is approximated as a deep trap state, its location within the band ultimately does not matter since one side of the junction trap states is deep and distorts the band structure to allow the leakage mechanisms to occur. This result further reinforces the notion that if the acceptor concentration is

on the order of the trap state concentration, they play a much more significant role than the trap state energy in determining the bending behavior around the TD.

D. Trap-assisted recombination dependence

Previous models have indicated that the leakage mechanism around TDs is related to carrier recombination near the intersection as shown by disk-shaped regions of high recombination rates in Figs. 7 and 11. To test this, a model with trap-associated lifetimes of 1 s was simulated to nullify the effect of trap state recombination at the interface. As can be seen in Fig. 12, the removal of SRH recombination at TD trap states does not completely remove leakage currents; but it does reduce them by almost an order of magnitude. In addition to the SRH recombination at the interface near the TD, the diffusion current of the junction alone near the TD also provides leakage current well over what would be expected in a perfect p-n diode. This effect can further be seen in Fig. 13. Although the SRH recombination at the TD trap states appears to have a significantly high leakage current in Fig. 12, Fig. 13 shows that the leakage current is largely caused by the depletion region and diffusion barrier reduction effects around the TD, for the leakage ratio of the no TD recombination diode over the ideal diode is approximately 10^4 at $V = 2.4 \text{ V}$ compared to 10 between the Control and the no TD recombination diode. With the absence of recombination at the trap states, the diffusive current component

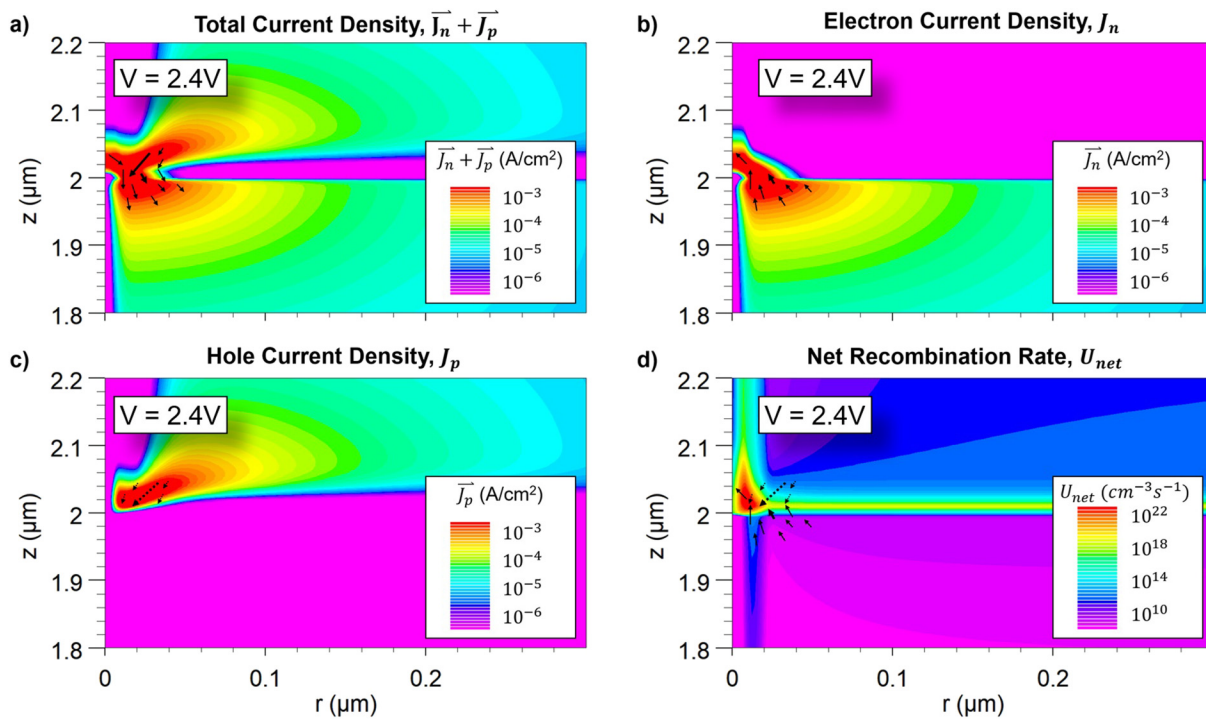


FIG. 11. n+p diode leakage current and recombination profiles. All plots are plotted using a log scale with the same magnitudes given in previous current density figures. (a) Total current density, (b) electron current density, (c) hole current density, and (d) net recombination rate.

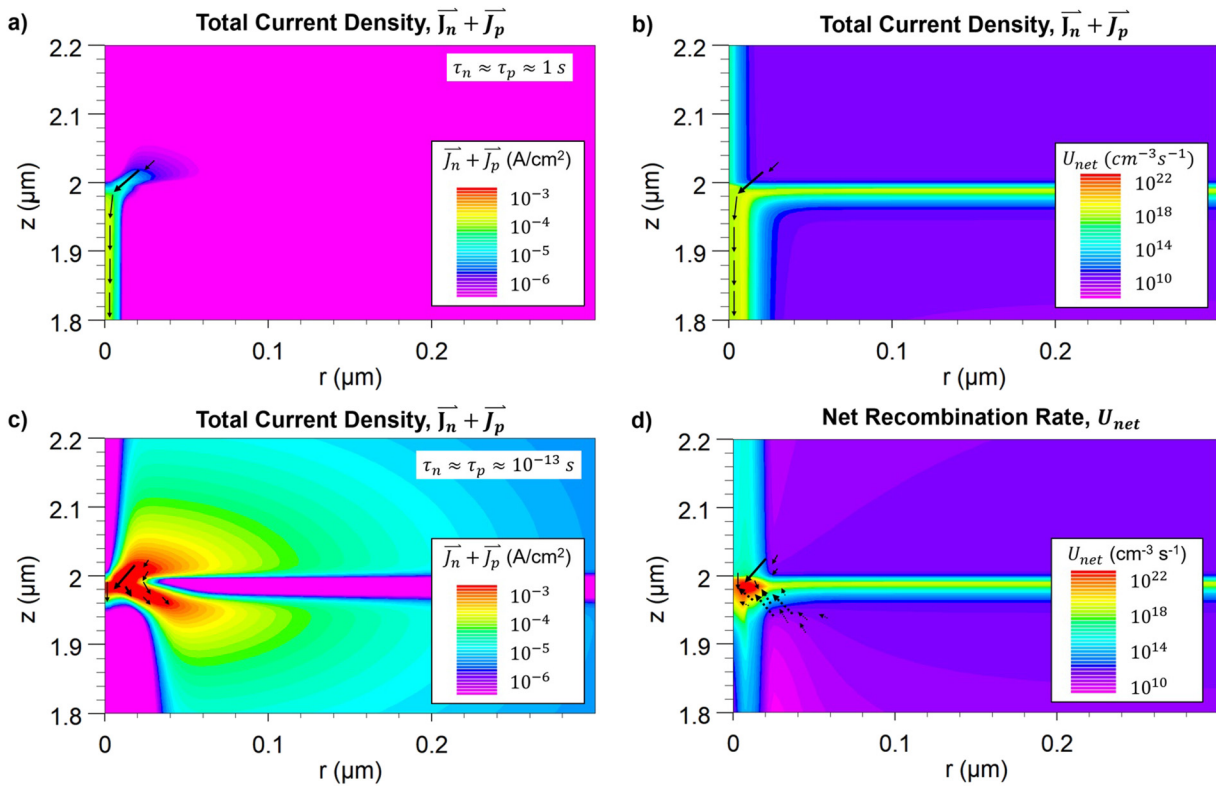


FIG. 12. Total current density colormaps highlighting the effect that the explicit, dislocation trap mediated carrier recombination has on the leakage current magnitude. (a) Total current density colormap of the diode with a 1 s carrier lifetime (thereby negating recombination effects of the dislocation trap states). Note that even without any trap state recombination, the dislocation screening region on the lightly doped side of the junction continues to mediate leakage current. (b) Total current density colormap of the control diode with 1 fs carrier lifetime. (c) Total current density colormap of the diode with a 10^{-13} s carrier lifetime. (d) Net recombination rate U_{net} .

of the Drift-Diffusion current model,

$$\vec{J}_n = qn\mu_n \vec{E}_n + \mathbf{qD}_n \nabla n, \quad (21)$$

is still greater than the drift component thereby allowing leakage

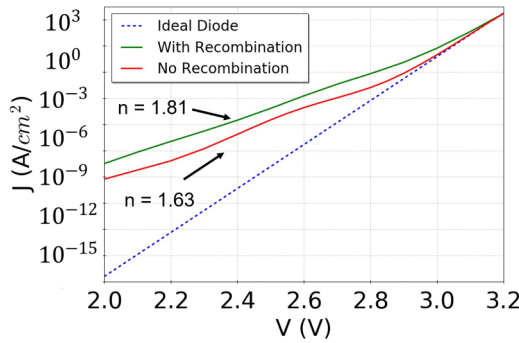


FIG. 13. J-V curves comparing the ideal, control, and no recombination diode models.

current to flow. However, the drift current still reduces the overall current by repelling carriers away from the intersection. By adding in trap state recombination, the drift component of the model becomes irrelevant as carriers do not need to fully cross the

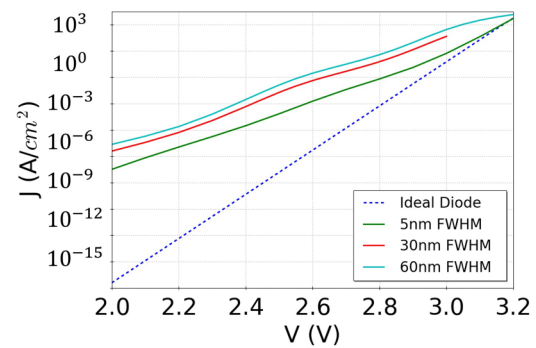


FIG. 14. J-V curves contrasting the effects of only the trap state distribution (hence screening region length) on the leakage current. This study differentiates the effects of only the screening geometry without changing the dislocation line charge or device doping.

depletion region. Instead, they simply need to overlap with the carriers diffusing from the other side of the junction at which point they rapidly recombine and create a much higher leakage current mediated by the depletion and barrier reduction and enhanced by the trap state recombination.

E. Isolated screening region geometry dependence

In addition to exploring the effect of screening region variance by controlling the doping in the junction, the screening region was also modified by changing the density profile of the TD-associated traps. These Gaussian FWHMs were modified to make them

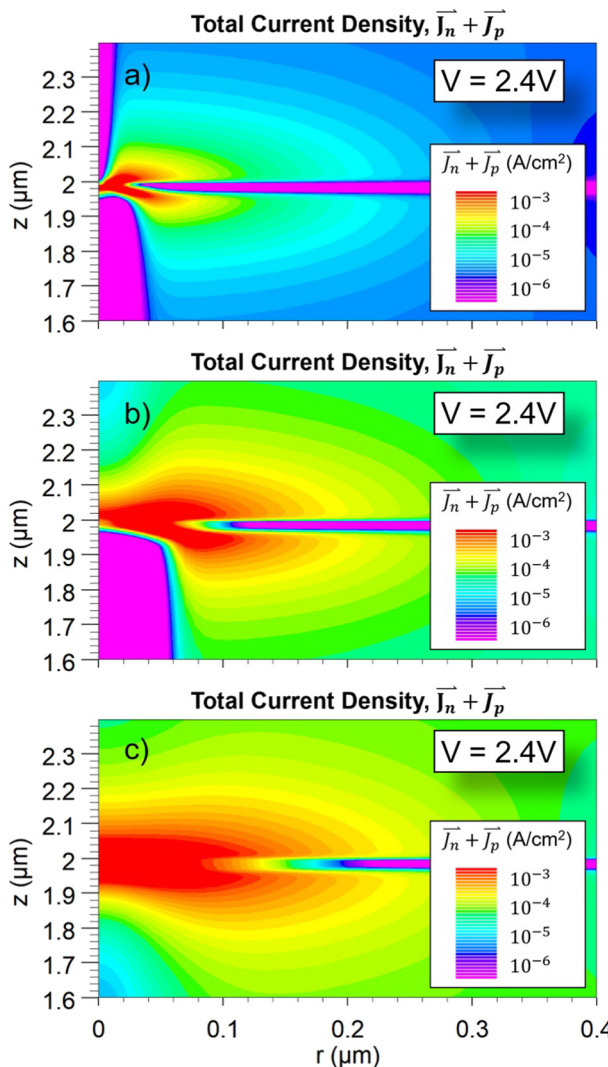


FIG. 15. Conduction current densities for various FWHM TD trap distributions with (a) the main model with an FWHM = 5 nm, (b) an FWHM = 30 nm, and (c) an FWHM = 60 nm.

broader, but the peak trap state densities were also changed such that an experimentally observed one electron per c-lattice translation was maintained. Although models were attempted with narrow trap state distributions, these led to numerical instability that prevent simulation convergence. In Fig. 14, the J-V curves of these broader trap state models are shown, and it can be clearly observed that the width of the distortions does contribute significantly to the forward bias leakage current.

With the reduced trap state densities, the effects previously seen on the trap occupancy in the lightly doped region of the diode are eliminated, yet leakage current not only persists but increases substantially. This indicates that the occupancy of the trap states does not play a major role in facilitating leakage since the trap states are fully occupied for these cases. Furthermore, in Fig. 15, we can see that the local magnitude of the leakage currents remains relatively unchanged with broader screening regions even as the total device current density increases. This indicates that the broader screening region interaction with the junction simply broadens the region over which diffusion current and SRH recombination can occur.

V. SUMMARY

This work has presented a 2D model of a *p-n* diode punctured by a distribution of trap states associated with dislocations in accordance with prior investigations^{26,40} and solved the Poisson-Drift-Diffusion system of equations using the Gummel method to determine the mechanisms by which dislocations mediate leakage. It was discovered that the dislocation trap states were ionized by the surrounding dopants and thus distorted the band in their vicinity with a heavy dependence on the doping density. This distortion of the energy bands results in a drastically reduced barrier to diffusion in forward bias, and this reduced diffusion barrier allows carriers to flow into a region of incredibly high recombination rates. It was discovered that regions around TDs in lightly doped semiconductors also inverted their majority carrier behavior that allowed leaked carriers to travel very far into the lightly doped region through the TD. The regions of barrier reduction, SRH recombination, and majority carrier inversion created by the distortion in the band structure result in observable leakage currents and increased ideality factors in GaN *p-n* junctions with dislocations.

ACKNOWLEDGMENTS

This research was supported the Solid State Lighting and Energy Electronics Center (SSLEEC) at UCSB and by ARPA-E PNDiodes Program through a subcontract from the University of New Mexico (I. Kizilyalli, program manager). Professor Yuh-Renn Wu was also funded by Ministry of Science and Technology (MOST) under No. 108-2628-E-002-010-MY3.

APPENDIX: REFERENCE TABLE

Table II is arranged in alphabetical order of the description with similar variables grouped together in the table (i.e., conduction, valence, and intrinsic energies are grouped together).

TABLE II. Variable legend providing detailed information on variables and units used in this work.

Sym.	Description	Value	Units
k	Boltzmann constant	8.62×10^{-5}	eV/K
σ_n	Capture cross section—electrons	1×10^{-12} (Ref. 22)	cm ²
σ_p	Capture cross section—holes	1×10^{-12} (Ref. 22)	cm ²
\bar{n}	Capture rate—electrons	N/A	s ⁻¹
\bar{p}	Capture rate—holes	N/A	s ⁻¹
N_A	Concentration—acceptor dopants	5×10^{19}	cm ⁻³
N_D	Concentration—donor dopants	5×10^{17}	cm ⁻³
n	Concentration—electrons	N/A	cm ⁻³
Q_T	Concentration—charged trap states	N/A	
p	Concentration—holes	N/A	cm ⁻³
n_i	Concentration—intrinsic carriers	3.43×10^{-10}	cm ⁻³
N_A^-	Concentration—ionized acceptor dopants	N/A	cm ⁻³
N_{tA}^-	Concentration—ionized acceptor traps	N/A	cm ⁻³
N_D^+	Concentration—ionized donor dopants	N/A	cm ⁻³
N_{ID}^+	Concentration—ionized donor traps	N/A	cm ⁻³
ρ_T	Concentration—trap states*	N/A	cm ⁻³
J_n	Current density—electrons	N/A	A/cm ²
J_p	Current density—holes	N/A	A/cm ²
ϵ_r	Dielectric constant	8.9	...
N_C	Effective density of states—conduction band	2.2×10^{18}	cm ⁻³
N_V	Effective density of states—valence band	4.2×10^{19}	cm ⁻³
m_n^*	Effective mass—electron	1.98×10^{-31} (0.2m ₀) (Ref. 41)	Kg
m_p^*	Effective mass—holes	1.28×10^{-30} (1.4m ₀) (Ref. 42)	Kg
ψ	Electric potential	N/A	V
q	Electron charge	1.61×10^{-19}	C
e_n	Emission rate—electrons	N/A	s ⁻¹
e_p	Emission rate—holes	N/A	s ⁻¹
E_A	Energy level – acceptor	0.19 ³⁴	eV
E_C	Energy level—conduction band edge	N/A	eV
E_D	Energy level—donor	0.025 ³⁴	eV
E_{Fn}	Energy level—electron quasi-Fermi	N/A	eV
E_{Fp}	Energy level—hole quasi-Fermi	N/A	eV
E_i	Energy level—intrinsic	1.73	eV
E_V	Energy level—valence band edge	N/A	eV
c	Lattice parameter—c-component	5.186	Å
τ_n	Lifetime—electrons	N/A	s
τ_p^{maj}	Lifetime—holes	N/A	s
μ_n^{maj}	Mobility—majority electrons	400	cm ² /Vs
μ_n^{min}	Mobility—minority electrons	32	cm ² /Vs
μ_p^{maj}	Mobility—majority holes	8	cm ² /Vs
μ_p^{min}	Mobility—minority holes	26	cm ² /Vs
ϵ_0	Permittivity of free space	8.85×10^{-14}	F/cm
U	Recombination rate—net	N/A	s ⁻¹
U_{SRH}	Recombination rate—Shockley-Read-Hall	N/A	s ⁻¹
R_{SC}	Screening radius	N/A	nm
g_n	State degeneracy—conduction band	2	...
g_p	State degeneracy—valence band	4	...
T	Temperature	300	K
v_n	Thermal velocity—electrons	2.60×10^7	cm/s
v_p	Thermal velocity—holes	9.87×10^6	cm/s
$f(E_T)$	Trap state occupancy	N/A	...

REFERENCES

- ¹C. Poblenz, P. Waltereit, S. Rajan, S. Heikman, U. K. Mishra, and J. S. Speck, *J. Vac. Sci. Technol. B* **22**, 1145 (2004).
- ²U. K. Mishra, L. Shen, T. E. Kazior, and Y.-F. Wu, *Proc. IEEE* **96**, 287 (2008).
- ³D. Denninghoff, J. Lu, M. Laurent, E. Ahmadi, S. Keller, and U. K. Mishra, in *70th Device Research Conference* (IEEE, 2012), pp. 151–152.
- ⁴S. W. Kaun, M. H. Wong, U. K. Mishra, and J. S. Speck, *Semicond. Sci. Technol.* **28**, 074001 (2013).
- ⁵B. Romanczyk, S. Wienecke, M. Guidry, H. Li, E. Ahmadi, X. Zheng, S. Keller, and U. K. Mishra, *IEEE Trans. Electron Devices* **65**, 45 (2018).
- ⁶T. Nishida, T. Makimoto, H. Saito, and T. Ban, *Appl. Phys. Lett.* **84**, 1002 (2004).
- ⁷P. Waltereit, H. Sato, C. Poblenz, D. S. Green, J. S. Brown, M. McLaurin, T. Katona, S. P. DenBaars, J. S. Speck, J.-H. Liang, M. Kato, H. Tamura, S. Omori, and C. Funaoka, *Appl. Phys. Lett.* **84**, 2748 (2004).
- ⁸R. Sharma, P. M. Pattison, H. Masui, R. M. Farrell, T. J. Baker, B. A. Haskell, F. Wu, S. P. DenBaars, J. S. Speck, and S. Nakamura, *Appl. Phys. Lett.* **87**, 231110 (2005).
- ⁹H. Sato, A. Tyagi, H. Zhong, N. Fellows, R. B. Chung, M. Saito, K. Fujito, J. S. Speck, S. P. DenBaars, and S. Nakamura, *Phys. Status Solidi (RRL)—Rapid Res. Lett.* **1**, 162 (2007).
- ¹⁰A. Tyagi, R. M. Farrell, K. M. Kelchner, C.-Y. Huang, P. S. Hsu, D. A. Haeger, M. T. Hardy, C. Holder, K. Fujito, D. A. Cohen, H. Ohta, J. S. Speck, S. P. DenBaars, and S. Nakamura, *Appl. Phys. Express* **3**, 011002 (2009).
- ¹¹D. A. Haeger, E. C. Young, R. B. Chung, F. Wu, N. A. Pfaff, M. Tsai, K. Fujito, S. P. DenBaars, J. S. Speck, S. Nakamura, and D. A. Cohen, *Appl. Phys. Lett.* **100**, 161107 (2012).
- ¹²S. Lee, C. A. Forman, C. Lee, J. Kearns, E. C. Young, J. T. Leonard, D. A. Cohen, J. S. Speck, S. Nakamura, and S. P. DenBaars, *Appl. Phys. Express* **11**, 062703 (2018).
- ¹³Y. Hatakeyama, K. Nomoto, N. Kaneda, T. Kawano, T. Mishima, and T. Nakamura, *IEEE Electron Device Lett.* **32**, 1674 (2011).
- ¹⁴I. C. Kizilyalli, A. P. Edwards, H. Nie, D. Disney, and D. Bour, *IEEE Trans. Electron Devices* **60**, 3067 (2013).
- ¹⁵T. Oka, T. Ina, Y. Ueno, and J. Nishii, *Appl. Phys. Express* **8**, 054101 (2015).
- ¹⁶O. Aktas and I. C. Kizilyalli, *IEEE Electron Device Lett.* **36**, 890 (2015).
- ¹⁷J. R. Dickerson, A. A. Allerman, B. N. Bryant, A. J. Fischer, M. P. King, M. W. Moseley, A. M. Armstrong, R. J. Kaplar, I. C. Kizilyalli, O. Aktas, and J. J. Wierer, *IEEE Trans. Electron Devices* **63**, 419 (2016).
- ¹⁸Y. Yoshizumi, S. Hashimoto, T. Tanabe, and M. Kiyama, *J. Cryst. Growth* **298**, 875 (2007).
- ¹⁹M. Qi, K. Nomoto, M. Zhu, Z. Hu, Y. Zhao, V. Protasenko, B. Song, X. Yan, G. Li, J. Verma, S. Bader, P. Fay, H. G. Xing, and D. Jena, *Appl. Phys. Lett.* **107**, 232101 (2015).
- ²⁰S. K. Mathis, A. E. Romanov, L. F. Chen, G. E. Beltz, W. Pompe, and J. S. Speck, *Phys. Status Solidi A* **179**, 125 (2000).
- ²¹S. K. Mathis, A. E. Romanov, L. F. Chen, G. E. Beltz, W. Pompe, and J. S. Speck, *J. Cryst. Growth* **231**, 371 (2001).
- ²²Z.-Q. Fang, D. C. Look, D. H. Kim, and I. Adesida, *Appl. Phys. Lett.* **87**, 182115 (2005).
- ²³E. C. H. Kyle, S. W. Kaun, P. G. Burke, F. Wu, Y.-R. Wu, and J. S. Speck, *J. Appl. Phys.* **115**, 193702 (2014).
- ²⁴D. Cherns, C. G. Jiao, H. Mokhtari, J. Cai, and F. A. Ponce, *Phys. Status Solidi B* **234**, 924 (2002).
- ²⁵I. Arslan and N. D. Browning, *Phys. Rev. B* **65**, 075310 (2002).
- ²⁶E. Müller, D. Gerthsen, P. Brückner, F. Scholz, T. Gruber, and A. Waag, *Phys. Rev. B* **73**, 245316 (2006).
- ²⁷D. C. Look and J. R. Sizelove, *Phys. Rev. Lett.* **82**, 1237 (1999).
- ²⁸E. C. H. Kyle, S. W. Kaun, E. C. Young, and J. S. Speck, *Appl. Phys. Lett.* **106**, 222103 (2015).
- ²⁹S. L. Rhode, M. K. Horton, W. Y. Fu, S.-L. Sahonta, M. J. Kappers, T. J. Pennycook, C. J. Humphreys, R. O. Dusane, and M. A. Moram, *Appl. Phys. Lett.* **107**, 243104 (2015).
- ³⁰S. Usami, N. Mayama, K. Toda, A. Tanaka, M. Deki, S. Nitta, Y. Honda, and H. Amano, *Appl. Phys. Lett.* **114**, 232105 (2019).
- ³¹S. Usami, Y. Ando, A. Tanaka, K. Nagamatsu, M. Deki, M. Kushimoto, S. Nitta, Y. Honda, H. Amano, Y. Sugawara, Y.-Z. Yao, and Y. Ishikawa, *Appl. Phys. Lett.* **112**, 182106 (2018).
- ³²K. Kumakura, T. Makimoto, N. Kobayashi, T. Hashizume, T. Fukui, and H. Hasegawa, *Appl. Phys. Lett.* **86**, 052105 (2005).
- ³³N. G. Weimann, L. F. Eastman, D. Doppalapudi, H. M. Ng, and T. D. Moustakas, *J. Appl. Phys.* **83**, 3656 (1998).
- ³⁴K. C. Collins, A. M. Armstrong, A. A. Allerman, G. Vizkelethy, S. B. Van Deusen, F. Léonard, and A. A. Talin, *J. Appl. Phys.* **122**, 235705 (2017).
- ³⁵S. Hafiz, F. Zhang, M. Monavarian, V. Avrutin, H. Morkoç, Ü Özgür, S. Metzner, F. Bertram, J. Christen, and B. Gil, *J. Appl. Phys.* **117**, 013106 (2015).
- ³⁶Z. Z. Bandić, P. M. Bridger, E. C. Piquette, and T. C. McGill, *Solid-State Electron.* **44**, 221 (2000).
- ³⁷M. Leroux, N. Grandjean, B. Beaumont, G. Nataf, F. Semond, J. Massies, and P. Gibart, *J. Appl. Phys.* **86**, 3721 (1999).
- ³⁸R. C. Jaeger and F. H. Gaenslen, *IEEE Trans. Electron Devices* **27**, 914 (1980).
- ³⁹J. G. Simmons and G. W. Taylor, *Phys. Rev. B* **4**, 502 (1971).
- ⁴⁰W. Shockley, *Bell Syst. Tech. J.* **28**, 435 (1949).
- ⁴¹W. Shockley and W. T. Read, *Phys. Rev.* **87**, 835 (1952).
- ⁴²C. A. Hurni, O. Bierwagen, J. R. Lang, B. M. McSkimming, C. S. Gallatin, E. C. Young, D. A. Browne, U. K. Mishra, and J. S. Speck, *Appl. Phys. Lett.* **97**, 222113 (2010).
- ⁴³L. Lymparakis, J. Neugebauer, M. Albrecht, T. Remmele, and H. P. Strunk, *Phys. Rev. Lett.* **93**, 196401 (2004).
- ⁴⁴I. Vurgaftman, J. R. Meyer, and L. R. Ram-Mohan, *J. Appl. Phys.* **89**, 5815 (2001).
- ⁴⁵A. Kasic, M. Schubert, S. Einfeldt, D. Hommel, and T. E. Tiwald, *Phys. Rev. B* **62**, 7365 (2000).